ACS Catalysis

Research Article

pubs.acs.org/acscatalysis

# $Mn_3O_4$ Supported on Glassy Carbon: An Active Non-Precious Metal Catalyst for the Oxygen Reduction Reaction

Yelena Gorlin,[†] Chia-Jung Chung,[‡] Dennis Nordlund,[§] Bruce M. Clemens,[‡] and Thomas F. Jaramillo*[,†]

[†]Department of Chemical Engineering and [‡]Department of Materials Science and Engineering, Stanford University, Stanford, California 94305, United States

[§]SLAC National Accelerator Laboratory, 2575 Sand Hill Rd, Menlo Park, California 94025, United States

Supporting Information

**ABSTRACT:** In this work, we explore the interplay between manganese oxide ($MnO_x$) nanomaterials and a glassy carbon (GC) support in catalyzing the oxygen reduction reaction (ORR) in an alkaline environment. Initially, we characterize the ORR activity of bare GC electrodes as a function of heat treatments in air, and find that ORR activity increases with increasing temperature up to 500 °C. Modification of GC with size-selected 1 nm $MnO_x$ nanoparticles prior to the 500 °C heat treatment yields a highly porous GC (pGC) structure, devoid of $MnO_x$. This pGC sample exhibits the highest ORR performance of the bare carbon electrodes reaching an onset potential of 0.75 V vs the reversible hydrogen electrode (RHE) and a complete 2-electron reduction of oxygen to peroxide. Having established ORR activity of bare GC electrodes, we deposit size-selected 14 nm MnO nanoparticles onto the GC and pGC electrodes and then incite phase changes in MnO through heat treatments in air. Electrochemical characterization of the resulting electrodes reveals that MnO nanoparticles offer no improvement in the ORR onset potential over bare GC or pGC and only slightly increase the number of electrons transferred. By contrast, thermal oxidation of MnO nanoparticles to $Mn_3O_4$ at 500 °C, confirmed by Mn L-edge X-ray absorption spectroscopy, results in an improved ORR onset potential of 0.80 V and a 4-electron reduction of oxygen. Thus at low overpotentials, where GC and pGC were inactive for the ORR, $MnO_x$ sites must contribute to all steps of the reaction. The catalyst's estimated specific activity of 3700 $\mu A \cdot cm^{-2}_{cat}$ at 0.75 V compares favorably with specific activities of Pt/C as well as the best nonprecious metal catalysts. This establishes $Mn_3O_4$ as another $MnO_x$ phase with high activity for the ORR.

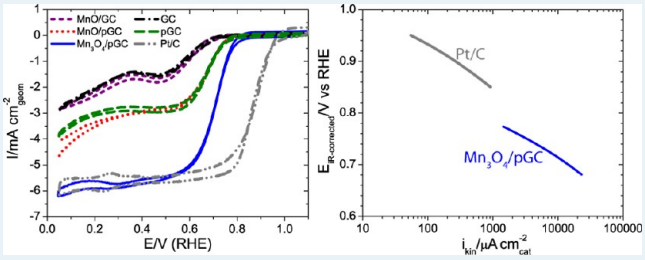


**KEYWORDS:** *oxygen reduction reaction, manganese oxide, glassy carbon, X-ray absorption spectroscopy, nanoparticles*

## INTRODUCTION

The oxygen reduction reaction (ORR) is an important reaction in cathodes of fuel cells and metal-air batteries. The current industry standard for ORR catalysts is nanoparticulate platinum supported on high surface area carbon,[1] but other high-performing catalysts consisting of nonprecious metal oxides, including $LaMnO_{3+\delta}$ and $LaNiO_3$ perovskites,[2] have been recently identified for catalysis in an alkaline environment. Manganese oxides ($MnO_x$) catalysts are another class of promising cathodes for alkaline fuel cells and metal-air batteries.[3] They are inexpensive, earth-abundant, environmentally benign, and can come in a variety of forms, many of which have been shown to have significant electrocatalytic activities for the 4-electron reduction of oxygen. Out of the $MnO_x$ characterized for the ORR, gamma-MnOOH,[4] alpha-$Mn_2O_3$,[5] alpha-$MnO_2$,[6,7] birnessite-$MnO_2$,[8] and beta-$MnO_2$,[9] have all been identified as high performing catalysts. Because of high activity of $MnO_x$ for peroxide disproportionation reaction,[10] it is possible for $MnO_x$ to catalyze 4-electron reduction of oxygen in combination with another material active for 2-electron reduction of oxygen to peroxide.[11]

Carbon electrodes, the most common supports for the ORR catalysts in cathodes of fuels and metal-air batteries,[10] have long been recognized as materials with high intrinsic activity for the electro-reduction of oxygen to peroxide.[10,12] Thus for $MnO_x$ catalysts supported on carbon, it is important to understand the roles of each material in catalyzing the ORR and the mechanistic pathways involved. Previous studies have linked the efficiency of the 2-electron reduction of oxygen on carbon to both the structure of the electrode and the various types of surface modifications.[13−15] Among the various forms of carbon, glassy carbon (GC) electrodes are known to have higher ORR activity than ordered carbon surfaces such as highly oriented pyrolitic graphite, likely because of a higher concentration of undercoordinated sites or oxidized carbon sites on the surface of the GC.[15] Modifications of the carbon surface through cleaning,[13,16,17] anodic polarization,[15,18,19] fracturing,[15] and heat treatment at reduced pressure[15,20] is associated with a further improvement in the overpotential for the ORR, while exposure

Received: July 3, 2012
Revised: September 11, 2012
Published: November 8, 2012

  

to atmosphere and electrolyte solutions leads to a gradual deactivation of the carbon surface.[13,16,21]

In our work, we explored the ORR activity of bare GC and GC supported $MnO_x$ electrodes as a function of heat treatments in air over a range of temperatures. Since previous studies have linked improvements in ORR activity of GC to heat treatment of the electrode at reduced pressure,[16,20] but identified exposure of GC to air as a contributing factor in deactivation of the electrode,[13,21] we initially focused on understanding the effect of thermal oxidation on the electrochemical activity of bare GC. After establishing the background ORR activity of thermally oxidized bare GC electrodes, we deposited $MnO_x$ nanoparticles onto various GC electrodes, manipulated the $MnO_x$ oxidation state through heat treatments in air, and then studied their activity for the ORR. Aiming to correlate the oxidation state of Mn in $MnO_x$ on GC with the ORR activity of the electrodes, we investigated the Mn valency using Mn L-edge X-ray absorption spectroscopy in addition to conventional X-ray photoelectron spectroscopy characterization. Our experiments identified $Mn_3O_4$ as a $MnO_x$ phase with 4-electron oxygen reduction activity for the ORR and an estimated specific activity of 3700 $\mu A \cdot cm^{-2}{}_{cat}$ at 0.75 V vs the reversible hydrogen electrode, a value that is extremely competitive with the best precious metal and nonprecious metal catalysts for the ORR in base.

## EXPERIMENTAL SECTION

**Preparation of GC Supports.** GC electrodes, polished to a surface roughness of less than 50 nm (0.196 $cm^2$, SigradurG), were purchased from HTW Hochtemperatur-Werkstoffe GmbH and subsequently heated in a quartz tube furnace (Mellen Company SC13) for 10 h at temperatures ranging from 250 to 500 °C.

**Synthesis of Nanoparticles.** $MnO_x$ nanoparticles were produced with a sputtering system (Nanosys500, Mantis Deposition Ltd.) using the inert gas condensation technique.[22,23] The deposition chamber consisted of the nanoparticle source and the quadrupole mass filter, which in situ filtered sputtered nanoparticles by mass. Selected nanoparticles were then deposited directly on the GC substrates in the main chamber, where the pressure was maintained at 0.3 mTorr with continuous Ar and He flow rates of 100 and 2 sccm. In this study, Mn nanoparticles were size selected at approximately 10 and 1 nm and deposited with a rate of either 0.16 $Å \cdot sec^{-1}$ or less than 0.01 $Å \cdot sec^{-1}$, monitored by a Quartz Crystal Microbalance (QCM). After deposition, samples were transferred to the load lock chamber and vented with Ar. To modify the oxidation state of the nanoparticles, a subset of manganese oxide nanoparticles was heat treated for 10 h in air at 500 °C in a quartz tube furnace (Mellen Company SC13).

**Physical and Chemical Characterization of Nanoparticles.** Size and morphology of the $MnO_x$ nanoparticles and GC support were determined using scanning electron microscopy (SEM, FEI Magellan 400XHR). The images were obtained using a secondary electron detector, a beam current of 25 pA, and beam voltage of 5 kV. The oxidation state of the $MnO_x$ nanoparticles was characterized using X-ray photoelectron spectroscopy (XPS, PHI 5000 VersaProbe) and X-ray absorption spectroscopy (XAS, Stanford Synchrotron Radiation Lightsource). Monochromatized Al K$\alpha$ 1486.6 eV X-rays were used to collect Mn 3s and C 1s X-ray photoelectron spectra on the samples and four $MnO_x$ powder standards (MnO, $Mn_3O_4$, $Mn_2O_3$, $MnO_2$; Sigma-Aldrich). Prior to collecting spectra on MnO, the powder was sputtered to remove the oxidized surface known to form on MnO in air.[24] All spectra were calibrated to 285.0 eV, the line position of adventitious carbon.[25] To acquire the spectra, a pass energy of 23.5 eV, an energy step of 0.1 eV, and a time of 20 ms per step were used; the corresponding resolution of the XPS measurement was 0.6 eV. Oxidation state of the $MnO_x$ nanoparticles was monitored using the relative magnitude of the 3s multiplet splitting ($\Delta E$3s), which has been previously shown to provide information on the oxidation state of Mn.[26,27]

XAS measurements were performed on the 31-pole wiggler beamline 10−1 at the Stanford Synchrotron Radiation Lightsource (SSRL) using a ring current of 350 mA and a 1000 $l \cdot mm^{-1}$ spherical grating monochromator with 40 $\mu$m entrance and exit slits, providing ~$10^{11}$ $ph \cdot s^{-1}$ at 0.3 eV resolution in a 1 $mm^2$ beam spot. All data were acquired in a single load at room temperature and under ultrahigh vacuum ($10^{-9}$ Torr) in total electron yield (TEY) mode, where the sample drain current was normalized by the current from freshly evaporated gold on a thin grid positioned upstream of the sample chamber. The measurements were performed on $MnO_x$ nanoparticles and three powder standards ($Mn_3O_4$, $Mn_2O_3$, $MnO_2$; Sigma-Aldrich) attached to an aluminum sample holder using conductive carbon. XAS spectra were not collected on the MnO powder because of surface oxidation in air during sample preparation.[24] The energy was carefully calibrated in two steps. First, all spectra were corrected for the drift in the beam energy by aligning the Mn L-edge spectra of a beamline reference sample, positioned upstream of the sample chamber to intercept a small part of the beam. We estimate that the resulting relative energy scale for all spectra is accurate within 50 meV. Second, the energy of the first peak of the $Mn_3O_4$ powder control was fixed to the literature value 639.6 eV,[24] and all spectra were shifted accordingly. Data were taken over the extended range of 610−690 eV to facilitate normalization. Normalization was performed by fitting a linear background to the spectra of all samples using the following two constraints: the area from 636 to 660 eV was specified to be the same in every spectrum and the edge jump in the 660 to 665 eV region of each spectrum was fixed to match the edge jump of $MnO_2$ powder standard.

**Electrochemical Characterization.** The electrochemical activities for the ORR of GC supports and $MnO_x$ nanoparticles were evaluated using cyclic voltammetry in a three electrode electrochemical cell in a rotating disk electrode configuration. Cyclic voltammograms (CVs) were collected in 0.1 M potassium hydroxide (KOH) electrolyte using a carbon rod counter electrode and Ag|AgCl reference electrode. The electrolyte was prepared from high purity KOH pellets (Sigma-Aldrich, 99.99%) and Millipore water. To account for the ohmic resistance of electrolyte, all CVs were *iR*-compensated to 85% during the measurements. Characterization was performed at room temperature (25 °C), 1600 rpm (rpm) rotation rate, and a sweep rate of 20 $mV \cdot s^{-1}$. The potential scale was calibrated to a reversible hydrogen electrode (RHE), and all potentials are reported vs RHE. RHE calibration was performed at the end of each characterization in a hydrogen saturated electrolyte with platinum catalyst at the working electrode. The potential at which the current crossed zero, which was approximately 0.960 V in all of the experiments, was taken to be the thermodynamic potential for the hydrogen electrode reactions. ORR activities were measured in oxygen saturated electrolyte in the potential region

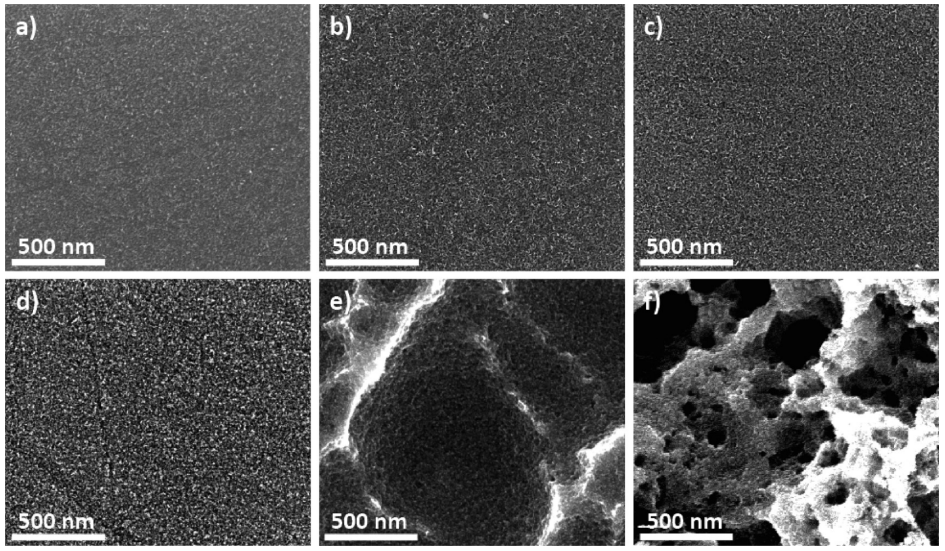


**Figure 1.** SEM images demonstrating morphologies of polished GC disks subjected to different heat treatments: (a) no heat treatment, (b) 250 °C, (c) 350 °C, (d) 450 °C, (e) 500 °C, (f) GC heat treated at 500 °C after having deposited 1 nm $MnO_x$ nanoparticles to form porous GC (pGC).

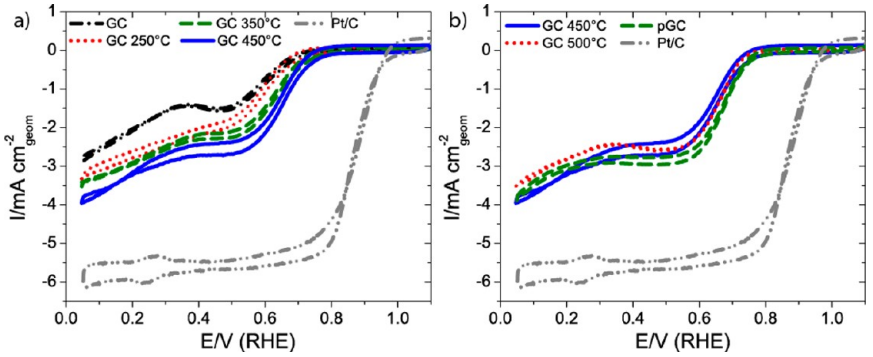


**Figure 2.** CVs of various GC electrodes and Pt/C nanoparticles obtained in oxygen saturated 0.1 M KOH electrolyte, at 20 $mV{\cdot}s^{-1}$ sweep rate, and 1600 rpm rotation rate. (a) Comparison of ORR activities of GC electrodes as a function of heat-treatment temperature demonstrates an increase in ORR activity as the temperature increases to 450 °C. (b) Further increase in temperature to 500 °C and the formation of the porous GC (pGC) morphology results in little change in ORR activities with GCs showing significantly lower onset potential and diffusion limited current than Pt/C nanoparticles.

between 0.05 and 1.1 V. Base CVs were recorded in the same potential window in nitrogen saturated environment to obtain capacitive contributions in the absence of oxygen. Two to five cyclic voltamograms were recorded for each catalytic material at each condition and the second or fourth CV is shown for each catalyst. The fourth CV is reported if the first two CVs were performed prior to complete saturation of the electrolyte with oxygen or nitrogen.

The ORR activities of GC electrodes and $MnO_x$ nanoparticles were compared to ORR activity of platinum nanoparticles supported on a high surface area carbon (46 wt % Pt/C, Tanaka Kikinzoku Kogyo). Pt/C catalyst inks were prepared using a standard procedure for fuel cell catalyst testing.[1] Briefly, 11.9 $\mu$g of Pt/C was ultrasonically dispersed in 6 mL of Millipore water, 4 mL of isopropanol, and 40 $\mu$L of nafion solution (5 wt %, Sigma-Aldrich), to achieve a concentration of 1.2 $mg_{pt}{\cdot}\mu L^{-1}$. Ten microliters of the catalyst ink was dropcast onto a GC disk mounted into an inverted RDE system, as recommended by Garsany and coauthors,[28] and dried for 45 min at 700 rpm to achieve a high quality Pt/C film on GC with a platinum loading of 28 $\mu g{\cdot}cm^{-2}$ on geometric surface area basis. Both the ORR activity and base CVs of the resulting catalyst were characterized using the procedure described above.

To determine the number of electrons transferred during the ORR on $MnO_x$ catalyst heat treated at 500 °C and Pt/C catalyst, a Koutecky–Levich analysis was carried out.[29] For the analysis, CVs were performed in an oxygen saturated environment under experimental conditions described above at 400, 900, and 1600 rpm rotation rates. Two to three CVs were collected at each rotation speed, as shown in Supporting Information, Figure S1. The inverse of the measured current of the last CV was plotted versus the inverse square root of the rotation rate at 0.65 V for $MnO_x$ catalyst and 0.85 V for Pt/C catalyst. The number of electrons, $n$, transferred during the reaction was extracted from the slope of the resulting plots using eq 1[29]

$$\text{slope} = \frac{1}{0.62nFD_{O_2}^{2/3}\nu^{-1/6}C_{O_2}} \quad (1)$$

where $F$ is Faraday's constant in $mA{\cdot}s{\cdot}mol^{-1}$, $D_{O_2}$ is the diffusion coefficient of oxygen in $cm^2{\cdot}s^{-1}$, $\nu$ is the kinematic viscosity in $cm^2{\cdot}s^{-1}$, $C_{O_2}$ is the solubility of oxygen in $mol{\cdot}cm^{-3}$,


dx.doi.org/10.1021/cs3004352 | ACS Catal. 2012, 2, 2687–2694

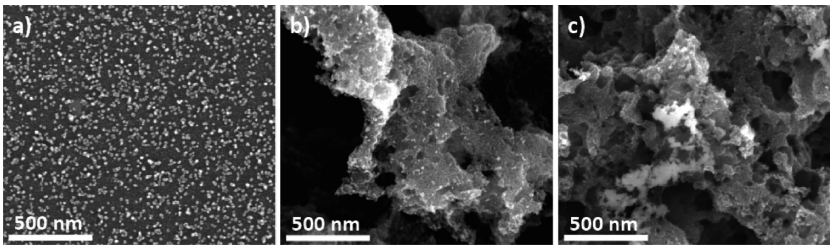


**Figure 3.** SEM images demonstrating the morphologies of $MnO_x$ on GC and pGC disks: (a) as-deposited size-selected 14 nm $MnO_x$ nanoparticles on GC, (b) as-deposited 14 nm $MnO_x$ nanoparticles on pGC, (c) agglomerated $MnO_x$ nanoparticles on pGC after a heat treatment at 500 °C.

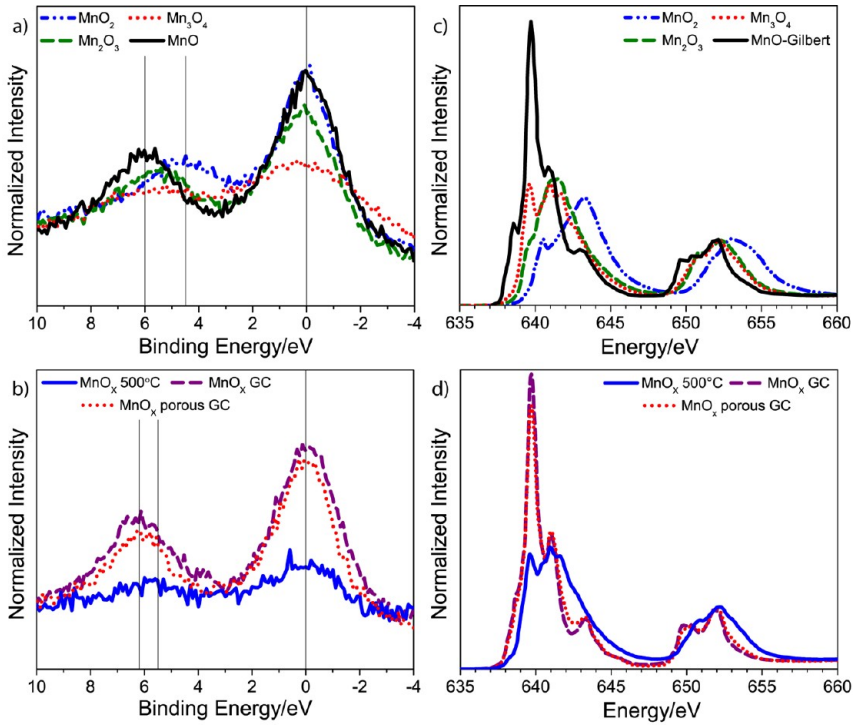


**Figure 4.** (a) Mn 3s XPS of powder standards plotted on a binding energy scale relative to the low binding energy multiplet. (b) Mn 3s XPS of $MnO_x$ catalysts demonstrating a decrease in the multiplet splitting after heat treatment at 500 °C. (c) Mn L-edge XAS spectra of $MnO_2$, $Mn_2O_3$, and $Mn_3O_4$ reference powder standards measured in our study and MnO data reproduced from Gilbert et al. and shifted by 0.5 eV. (d) Mn L-edge XAS spectra of as-deposited $MnO_x$ nanoparticles on GC, as-deposited $MnO_x$ nanoparticles on pGC, and $MnO_x$ nanoparticles on GC after heat treatment at 500 °C. This data confirms the thermal oxidation of MnO nanoparticles to $Mn_3O_4$, yielding samples denoted from now on as MnO/GC, MnO/pGC, and $Mn_3O_4$/pGC.

and $w$ is the rotation rate of the rotating disk electrode in rad·$s^{-1}$. In 0.1 M KOH electrolyte at room temperature (25 °C), $D_{O_2}$, $\nu$, and $C_{O_2}$ are 1.85 × $10^{-5}$ $cm^2 \cdot s^{-1}$,[30] 0.89 × $10^{-2}$ $cm^2 \cdot s^{-1}$,[31] and 1.21 × $10^{-6}$ mol·$cm^{-3}$.[30]

## RESULTS AND DISCUSSION

To investigate the effect of thermal oxidation on the electrochemical activity of bare GC electrodes, we heat treated GCs at 250 °C, 350 °C, 450 °C, and 500 °C in air. The morphology of the disks prior to heat treatment and after these heat treatments is shown in Figure 1, panels a–e. Only subtle changes in the surface morphology are observed up to and including 450 °C. After heat-treatment at 500 °C the surface visibly roughens to form craters in the GC because of corrosion of carbon and evolution of CO and $CO_2$ gases.[20,32] We found that addition of catalytic material onto GC prior to heat treatment resulted in even greater corrosion of the electrode. Specifically, deposition of ∼1 nm manganese oxide ($MnO_x$) nanoparticles and subsequent heat treatment at 500 °C produced significant gas evolution from the surface, forming a highly porous carbon morphology shown in Figure 1f. X-ray photoelectron spectroscopy (XPS) characterization of this particular surface revealed that no $MnO_x$ was left on the surface (Supporting Information, Figure S2). We will refer to this particular form of heat-treated carbon (with $MnO_x$ deposited prior to the 500 °C heat treatment), as porous GC (pGC).

Electrochemical activity of the bare GC supports for the ORR measured in an oxygen-saturated 0.1 M KOH electrolyte at 1600 rpm is shown in Figure 2, panels a and b. Figure 2a shows that the catalytic activity improved with increasing heat treatment temperature up to 450 °C, as noted by the decrease in overpotential required for the electro-reduction of oxygen to peroxide. For the sample heat treated at 450 °C, the electrode demonstrated close to complete 2-electron reduction to $OOH^-$ by reaching the expected diffusion limited current of 2.9 mA/$cm^2$ (see Supporting Information for the calculation of the theoretical diffusion limited current). GC surfaces with visibly roughened morphologies because of heat treatment at 500 °C,


dx.doi.org/10.1021/cs3004352 | ACS Catal. 2012, 2, 2687–2694

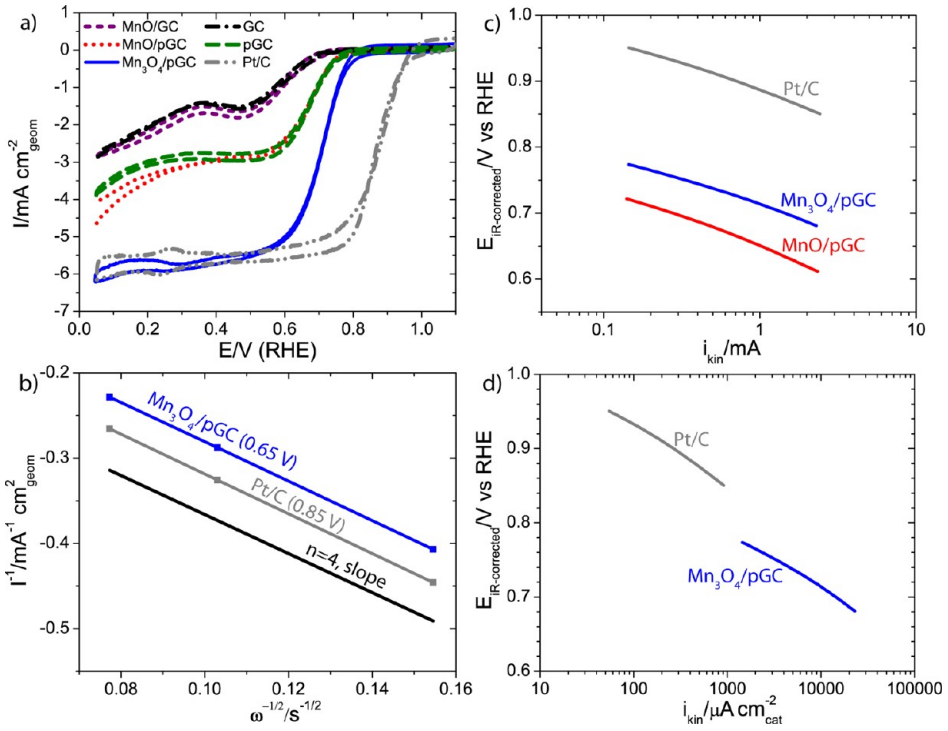


**Figure 5.** (a) CVs of six samples: MnO/GC, MnO/pGC, $Mn_3O_4$/pGC, bare GC, bare pGC, and nanoparticulate Pt/C, all measured in oxygen saturated 0.1 M KOH electrolyte, at a 20 mV·s$^{-1}$ sweep rate and 1600 rpm rotation rate. (b) Koutecky–Levich analysis of $Mn_3O_4$/pGC and Pt/C demonstrates 4. (c) Tafel plots of kinetic current for MnO/pGC, $Mn_3O_4$/pGC, and Pt/C constructed after correcting the potential for uncompensated ohmic losses and capacitive current obtained in $N_2$ scans and removing mass-transport losses from the measured current. (d) Normalization of Tafel plots by estimated surface areas of $Mn_3O_4$ and Pt to determine specific activities of the catalysts as a function of applied potential.

both with and without the addition of a small amount of $MnO_x$ prior to heating, exhibit similar activities to the catalyst heat treated at 450 °C, as observed in Figure 2b. At about 0.35 V, all carbon surfaces show an onset of another reduction process, likely corresponding to the subsequent 2 $e^-$ conversion of peroxide to water.[4] The favorable effect of thermal oxidation on the ORR activity of GCs was consistent with previous studies that had reported an improvement in both the onset potential and the number of electrons transferred on electrochemically oxidized GCs.[15,18,19]

After characterization of the baseline ORR activity of the various GC electrodes, size-selected $MnO_x$ nanoparticles of approximately 14 nm in diameter were deposited onto either GC or pGC and further processed to form the following set of samples: (1) as-deposited $MnO_x$ catalyst on GC, (2) as-deposited $MnO_x$ catalyst on pGC, and (3) an $MnO_x$ catalyst deposited onto GC and subsequently heat treated at 500 °C. The 500 °C heat treatment was expected to induce a phase change in the $MnO_x$ catalyst as well as a morphological change in the carbon support to form pGC. SEM images of these three samples are shown in Figure 3, panels a, b, c, respectively. Figures 3a and 3b show that with no heat treatment the $MnO_x$ nanoparticles were well dispersed (i.e., minimal agglomeration) on both the GC and the pGC supports, respectively. A surface coverage of approximately 12% was determined for these two samples. For the third sample, which underwent the 500 °C heat treatment, the $MnO_x$ nanoparticles had agglomerated substantially, forming thin-film like particles several hundred nm wide as observed in Figure 3c. Since a sample with smaller $MnO_x$ nanoparticles of 1 nm diameter resulted in a structure devoid of all manganese oxide after the same heat treatment, it is likely that some $MnO_x$ material of the 14 nm size-selected clusters was lost during the heating step. The oxidation state of Mn in the three samples was first studied using XPS. Mn 3s XPS spectra of four well-defined powder standards (MnO, $Mn_3O_4$, $Mn_2O_3$, and $MnO_2$) as well as the three $MnO_x$/GC samples are shown in Figures 4a and 4b, respectively, plotted on a binding energy scale relative to the low binding energy multiplet. The magnitude of the 3s multiplet splitting ($\Delta E$3s) in the Mn XPS spectra of powder standards decreased from 6.0 to 4.5 eV as the oxidation state increased from Mn(II) of MnO to Mn(IV) of $MnO_2$, in agreement with the reported $\Delta E$3s splitting as a function of formal valence.[26,27] Both the as-deposited $MnO_x$/GC sample and the as-deposited $MnO_x$/pGC sample exhibited $\Delta E$3s multiplet splittings of 6.2 eV, consistent with MnO. This suggests that MnO is the native form of $MnO_x$ produced by the cluster source in the 14 nm size regime. Heat-treatment of the MnO nanoparticles resulted in a decrease in the splitting value from about 6.2 eV to about 5.5 eV, indicating an increase in the oxidation state from Mn(II) to a valency closer to 3+,[33] but detailed information on the oxidation state and coordination could not be extracted from the XPS results. To better understand the catalyst structure, we turned to synchrotron methods, specifically XAS.

Mn L-edge XAS is a sensitive probe of Mn oxidation state and coordination.[34−36] In Figure 4c we show Mn L-edge XAS spectra of the three reference powder samples ($MnO_2$, $Mn_2O_3$, and $Mn_3O_4$) measured in our study as well as that of MnO, a sputtered sample without any oxidized surface contribution, reproduced from Gilbert et al. (shifted by 0.5 eV).[24] The four different types of $MnO_x$ have distinct L-edge spectra, allowing for a straightforward differentiation between possible oxidation


dx.doi.org/10.1021/cs3004352 | ACS Catal. 2012, 2, 2687−2694

states of $MnO_x$. As observed in Figure 5d, the spectrum of the heat treated sample is in excellent agreement with the spectrum of $Mn_3O_4$ powder, while the spectra of the as-deposited nanoparticles on GC and pGC are nearly identical to the spectrum of MnO by Gilbert et al.,[24] revealing a Mn (II) oxidation state with a very small surface oxidation contribution. XAS measurements thus confirm the oxidation of the nanoparticles during the heat treatment at 500 °C and elucidate the specific starting and ending phases as MnO and $Mn_3O_4$, respectively. It is worthy to note that for bulk $MnO_x$, the expected phase at 500 °C in air is alpha-$Mn_2O_3$ and not $Mn_3O_4$.[26,37] $MnO_x$ phase behavior, however, has been previously shown to be size-dependent, with smaller particles favoring the formation of $Mn_3O_4$, the phase with a lower surface energy.[38] Thus, the observed formation of $Mn_3O_4$ at 500 °C can be explained in part by the nanoparticulate nature of the sample.

The ORR activities of the three carbon-supported $MnO_x$ samples are shown in Figure 5a along with ORR activities of bare GC, bare pGC, and the Tanaka Pt/C catalyst for comparison. The MnO/GC and MnO/pGC samples offer little, if any, improvement in the ORR activity over the baseline activities of their respective bare carbon surfaces. More specifically, in the kinetic region the ORR current densities of the MnO/GC and MnO/pGC samples overlap those of their respective bare carbon surfaces, while in the diffusion limited region only a slight enhancement in the ORR current is observed. This result is consistent with previous literature studies that have not observed greater than 2-elecron reduction of oxygen on MnO.[9,39] Thermal oxidation of MnO nanoparticles to $Mn_3O_4$ and concomitant conversion in carbon morphology to pGC results in a significant improvement in ORR activity, as measured by a 50 mV decrease in the overpotential for $O_2$ reduction and an increase in diffusion limited current to 5.7 mA/cm$^2$, the theoretical diffusion limited current for 4-electron reduction of oxygen (see Supporting Information for calculation details). Koutecky−Levich analysis of the ORR on $Mn_3O_4$/pGC and Pt/C, shown in Figure 5b, confirms that the reaction proceeds through 4-electron reduction on both catalysts. The significant improvement both in the onset potential and the number of electrons transferred displayed by $Mn_3O_4$/pGC over the bare pGC substrate demonstrates that the $Mn_3O_4$ phase has high activity for the ORR. Several research groups have previously investigated the activity of $Mn_3O_4$ for the ORR,[4,9,40−45] demonstrating that the catalyst is capable of reaching between 2 and 3-electron reduction of oxygen on both gold[40] and carbon[9,41,43] supports, with onset potentials of 0.75−0.85 V.[4,9,40,41,43,45] A recent theoretical study has also predicted $Mn_3O_4$ to be among active $MnO_x$ phases for the 4-electron reduction of oxygen with ORR activity similar to that of beta-$MnO_2$ and alpha-$Mn_2O_3$.[46] Our $Mn_3O_4$/pGC catalyst matches the expected onset potentials for the ORR as predicted by theory and, for the first time, demonstrates a complete 4-electron reduction of oxygen on a $Mn_3O_4$ phase.

To gain a better understanding of the kinetics of the ORR on MnO/pGC and $Mn_3O_4$/pGC, Tafel plots were constructed by plotting the logarithm of the kinetic current vs the *iR*-corrected potential for the two $MnO_x$ catalysts and Pt/C nanoparticles. To extract kinetic current of the catalytic materials, several corrections were applied to the ORR CVs. First, the potential was compensated for the remaining 15% of ohmic resistance of the electrolyte, which was approximately 40 Ω for all samples. Second, the ORR CVs were adjusted for capacitive contributions using $N_2$ scans, shown in Supporting Information, Figure S3, obtained in the same potential window and under the same conditions as the ORR CVs. The kinetic current was then calculated by correcting for mass transport losses using eq 2,

$$\frac{1}{i_m} = \frac{1}{i_k} + \frac{1}{i_d} \tag{2}$$

where $i_m$ refers to the measured current in the ORR CV in anodic direction corrected for ohmic resistance and capacitance current, $i_k$ refers to the kinetic current, and $i_d$ refers to the diffusion limited current obtained experimentally. As seen in Figure 5c, the Tafel slopes of the MnO/pGC and $Mn_3O_4$/pGC catalysts are similar to that of Pt/C in the range of 80−90 mV·decade$^{-1}$. The calculated kinetic current was normalized by the estimated surface areas of $Mn_3O_4$ and Pt to calculate specific activities of the two catalysts. The upper bound value of the surface area of $Mn_3O_4$ catalyst was estimated to be 0.1 cm$^2$ from SEM images of the nanoparticles prior to heat treatment (Supporting Information, Figure S4). We stress that this value is an upper bound, as after the heat treatment the particles have agglomerated and will likely have substantially lower surface area than the starting nanoparticles. The surface area of Pt/C nanoparticles was calculated to be 2.65 cm$^2$ using an established procedure which involves the measurement of the charge from the electrochemical hydrogen underpotential deposition (HUPD) and then determining the electrochemically active surface area based on 210 $\mu$C·cm$^{-2}{}_{Pt}$.[1,47] The details of the surface area calculations are provided in the Supporting Information. The resulting specific activity and the corresponding mass activity plots, shown in Figures 5d and Supporting Information, Figure S5, demonstrate that the ORR activity of $Mn_3O_4$/pGC catalyst, with a loading of 0.1 $\mu$g·cm$^{-2}$ (1.4 nmol·cm$^{-2}$), compares favorably with the ORR activity of the Pt/C catalyst, despite the later ORR onset potential of $Mn_3O_4$/pGC. Considering that a higher loading of 3.5 $\mu$g·cm$^{-2}$ (17.9 nmol·cm$^{-2}$) is necessary for platinum in nanoparticulate Pt/C catalysts to achieve 4-electron reduction of oxygen in a RDE configuration,[48] the ability of the $Mn_3O_4$/pGC to catalyze the 4-electron reduction of oxygen is exceptional. The outstanding ORR performance of the $Mn_3O_4$/pGC catalyst is further evidenced by comparing its specific activity of 3700 $\mu$A·cm$^{-2}{}_{cat}$ and the corresponding mass activity of 3100 A·g$^{-1}{}_{cat}$, both measured at 0.75 V, to the best reported $MnO_x$ catalysts (Supporting Information, Table S1)[5−9,40,41] and the best non-noble metal catalysts reported in literature.[2] The specific activity of the $Mn_3O_4$/pGC catalyst at 0.75 V vs RHE is 1−2 orders of magnitude higher than the specific of activities of the majority of high-performance manganese oxide and perovskite ORR catalysts and is of the same order of magnitude as the best reported nonprecious metal catalysts in alkaline media, $LaMnO_{3+\delta}$ and $LaNiO_3$.[2]

Having established the outstanding ORR activity of the $Mn_3O_4$/pGC catalyst, we turn our attention to mechanistic possibilities for oxygen reduction on this electrode. The overall 4-electron ORR in basic electrolyte is shown in eq 3. This can be achieved by a direct pathway or a series pathway involving a peroxide intermediate.[10] The direct pathway proceeds through a sequence of steps such that all four electron transfers of eq 3 occur on the same catalytic site. In the series pathway, there is an initial 2-electron reduction of oxygen to peroxide (eq 4), likely proceeding in two distinct electron-transfer steps (not


dx.doi.org/10.1021/cs3004352 | ACS Catal. 2012, 2, 2687−2694

shown), followed by one of two possibilities: either a 2-electron reduction step of peroxide to water (eq 5a) or the peroxide disproportionation reaction (eq 5b) that produces $O_2$ in half the original amount via a chemical and not electrochemical step. This $^1/_2O_2$ is subsequently reduced back to peroxide with eqs 4 and 5b cycled repeatedly until reaching a theoretical limit of an overall 4-electron process $(2 + 1 + 1/2 + 1/4 + \cdots \approx 4)$.[10] In the series pathway, it is plausible that two completely different catalytic sites can participate in the reactions 4 and 5a/5b.

$$O_2 + 2H_2O + 4e^- \rightarrow 4OH^- \quad (3)$$

$$O_2 + H_2O + 2e^- \rightarrow OOH^- + OH^- \quad (4)$$

$$OOH^- + H_2O + 2e^- \rightarrow 3OH^- \quad (5a)$$

$$OOH^- \rightarrow \frac{1}{2}O_2 + OH^- \quad (5b)$$

While the subject of ORR mechanisms on $MnO_x$ based catalysts is still being explored, several research groups have proposed a series pathway consisting of reactions 4 and 5b as the likely mechanism.[4,7,9,10,40,41] In this particular pathway, reaction 4 has been shown to occur either on the electrode support onto which $MnO_x$ is deposited, such as carbon or gold,[4,11,40] or on Mn(IV)/Mn(III) sites of $MnO_x$,[9,49] while the catalytic activity for reaction 5b has been attributed to $MnO_x$.[1,4,6,9,38,39] In our work on the $Mn_3O_4$/pGC catalyst, we recognize that at potentials cathodic of 0.75 V, the exposed bare sites of the pGC support will likely contribute catalytically to the initial 2-electron reduction since a bare porous GC electrode demonstrated high activity for 2-electron reduction of oxygen at these potentials. At a potential of 0.75 V exactly, where no appreciable current is yet observed on a bare pGC electrode, $MnO_x$ sites must be involved in all steps of the reaction, irrespective of the pathway. We note, however, that the pGC support could still be contributing to the observed catalytic activity in other, indirect ways, for instance by tuning the electronic or geometric structure of the $MnO_x$, or perhaps through a bifunctional mechanism where atomically adjacent $MnO_x$ and C sites participate in turning over an adsorbed molecule at that particular interface. Further experiments, which investigate the effect of surface coverage by $Mn_3O_4$, could provide information on the role of pGC in producing high catalytic activity.

The morphology of the GC support could also play a critical role in producing the exceptional catalytic activity observed on this $Mn_3O_4$/pGC catalyst. For example, the porous electrode may trap peroxide intermediates and thus facilitate the disproportionation pathway.[50,51] This could potentially be probed in a future study by quantifying the amount of peroxide formed as a function of the porosity of the GC support or by changing the hydrophobicity of the support,[52] assuming that the same $Mn_3O_4$ phase and morphology can be maintained. As porous carbon is a common support material both in fuel cells and metal-air batteries,[10] further elucidation of the contribution of pGC to the ORR activity of $Mn_3O_4$ phase could aid in the design of active electrodes for energy storage and energy conversion technologies.

## CONCLUSIONS

In this work, we investigated the interplay between manganese oxide ($MnO_x$) and GC supports in catalyzing the ORR in alkaline media. We studied the ORR activity of thermally oxidized bare GC electrodes, which formed a highly porous structure (pGC) under certain preparation conditions, as well as that of $MnO_x$/GC and $MnO_x$/pGC electrodes to probe the effects of $MnO_x$ phase and GC morphology. We demonstrated that heat treatment of bare GC in air at 500 °C resulted in an improvement in ORR onset potential from 0.70 to 0.75 V and a complete 2-electron reduction of oxygen to peroxide. Among the various $MnO_x$/GC and $MnO_x$/pGC catalysts studied, we found that size-selected MnO nanoparticles of 14 nm diameter did not improve the onset potential for the reaction beyond that of what was expected from the bare carbon supports, and only slightly increased the number of electrons transferred in the diffusion limited current region. Upon thermal oxidation, the MnO nanoparticles were converted to $Mn_3O_4$, while the carbon support formed a porous structure, pGC. The resulting $Mn_3O_4$/pGC electrode exhibited a significant enhancement in catalytic activity. The onset potential improved to 0.80 V and a complete 4-electron reduction of oxygen was observed. At 0.75 V, the $Mn_3O_4$/pGC catalyst's measured specific and mass activities of 3700 $\mu A \cdot cm^{-2}_{cat}$ and 3100 $A \cdot g^{-1}_{cat}$ represent an extremely high performing catalyst; these values compare favorably to those of the best non-noble metal catalysts and even to that of a state-of-the-art nanoparticulate Pt/C catalyst. Given the absence of ORR activity by bare pGC at 0.75 V, these results indicate that at low overpotentials $MnO_x$ sites participate in all steps of the reaction. Our electrochemical results in combination with L-edge X-ray absorption spectroscopy characterization establish $Mn_3O_4$ as a $MnO_x$ phase with high activity for the ORR.

## ASSOCIATED CONTENT

### Supporting Information

XPS survey scan of porous GC substrate, $N_2$ CVs, determination of the surface area of catalytic materials, calculation of the theoretical diffusion limited current, and mass activity of Pt/C and $Mn_3O_4$/pGC. This material is available free of charge via the Internet at http://pubs.acs.org.

## AUTHOR INFORMATION

### Corresponding Author

*E-mail: jaramillo@stanford.edu.

### Notes

The authors declare no competing financial interest.

## ACKNOWLEDGMENTS

This material is based upon work supported as part of the Center on Nanostructuring for Efficient Energy Conversion (CNEEC) at Stanford University, an Energy Frontier Research Center funded by the U.S. Department of Energy, Office of Science, Office of Basic Energy Sciences under Award Number DE-SC0001060. XAS characterization was carried out at the Stanford Synchrotron Radiation Lightsource, a Directorate of SLAC National Accelerator Laboratory and an Office of Science User Facility operated for the U.S. Department of Energy Office of Science by Stanford University. The SSRL Structural Molecular Biology Program is supported by the DOE Office of Biological and Environmental Research, and by the National Institutes of Health, National Center for Research Resources, Biomedical Technology Program (P41RR001209).

## REFERENCES


(1) Gasteiger, H. A.; Kocha, S. S.; Sompalli, B.; Wagner, F. T. *Appl. Catal., B* **2005**, *56* (1−2), 9−35.
(2) Suntivich, J.; Gasteiger, H. A.; Yabuuchi, N.; Nakanishi, H.; Goodenough, J. B.; Shan-Horn, Y. *Nat. Chem.* **2011**, *3* (7), 546−550.
(3) Cheng, F. Y.; Chen, J. *Chem. Soc. Rev.* **2012**, *41* (6), 2172−2192.
(4) Mao, L. Q.; Sotomura, T.; Nakatsu, K.; Koshiba, N.; Zhang, D.; Ohsaka, T. *J. Electrochem. Soc.* **2002**, *149* (4), A504−A507.
(5) Gorlin, Y.; Jaramillo, T. F. *J. Am. Chem. Soc.* **2010**, *132* (39), 13612−13614.
(6) Xiao, W.; Wang, D. L.; Lou, X. W. *J. Phys. Chem. C* **2010**, *114* (3), 1694−1700.
(7) Cheng, F. Y.; Su, Y.; Liang, J.; Tao, Z. L.; Chen, J. *Chem. Mater.* **2010**, *22* (3), 898−905.
(8) Cao, Y. L.; Yang, H. X.; Ai, X. P.; Xiao, L. F. *J. Electroanal. Chem.* **2003**, *557*, 127−134.
(9) Lima, F. H. B.; Calegaro, M. L.; Ticianelli, E. A. *Electrochim. Acta* **2007**, *52* (11), 3732−3738.
(10) Yeager, E. *J. Mol. Catal.* **1986**, *38* (1−2), 5−25.
(11) El-Deab, M. S.; Ohsaka, T. *J. Electrochem. Soc.* **2006**, *153* (7), A1365−A1371.
(12) Garten, V. A.; Weiss, D. E. *Aust. J. Chem.* **1955**, *8* (1), 68−95.
(13) Sljukic, B.; Banks, C. E.; Compton, R. G. *J. Iran. Chem. Soc.* **2005**, *2* (1), 1−25.
(14) Bowling, R. J.; Packard, R. T.; McCreery, R. L. *J. Am. Chem. Soc.* **1989**, *111* (4), 1217−1223.
(15) Xu, J.; Huang, W. H.; McCreery, R. L. *J. Electroanal. Chem.* **1996**, *410* (2), 235−242.
(16) Hu, I. F.; Karweik, D. H.; Kuwana, T. *J. Electroanal. Chem.* **1985**, *188* (1−2), 59−72.
(17) Yang, H. H.; McCreery, R. L. *J. Electrochem. Soc.* **2000**, *147* (9), 3420−3428.
(18) Engstrom, R. C.; Strasser, V. A. *Anal. Chem.* **1984**, *56* (2), 136−141.
(19) Nagaoka, T.; Sakai, T.; Ogura, K.; Yoshino, T. *Anal. Chem.* **1986**, *58* (9), 1953−1955.
(20) Stutts, K. J.; Kovach, P. M.; Kuhr, W. G.; Wightman, R. M. *Anal. Chem.* **1983**, *55* (9), 1632−1634.
(21) Rusling, J. F. *Anal. Chem.* **1984**, *56* (3), 575−578.
(22) Yamada, I.; Usui, H.; Takagi, T. *Z. Phys., D: At. Mol. Clusters* **1986**, *3* (2−3), 137−142.
(23) Ayesh, A. I.; Qamhieh, N.; Ghamlouche, H.; Thaker, S.; El-Shaer, M. *J. Appl. Phys.* **2010**, *107* (3), 034317.
(24) Gilbert, B.; Frazer, B. H.; Belz, A.; Conrad, P. G.; Nealson, K. H.; Haskel, D.; Lang, J. C.; Srajer, G.; De Stasio, G. *J. Phys. Chem. A* **2003**, *107* (16), 2839−2847.
(25) Barr, T. L.; Seal, S. *J. Vac. Sci. Technol., A* **1995**, *13* (3), 1239−1246.
(26) Dicastro, V.; Polzonetti, G. *J. Electron Spectrosc. Relat. Phenom.* **1989**, *48* (1−2), 117−123.
(27) Foord, J. S.; Jackman, R. B.; Allen, G. C. *Philos. Mag. A* **1984**, *49* (5), 657−663.
(28) Garsany, Y.; Singer, I. L.; Swider-Lyons, K. E. *J. Electroanal. Chem.* **2011**, *662* (2), 396−406.
(29) Bard, A. J.; Faulkner, L. R., *Electrochemical Methods: Fundamentals and Applications*, 2 ed.; Wiley: New York, 2000; pp 339−341.
(30) Davis, R. E.; Horvath, G. L.; Tobias, C. W. *Electrochim. Acta* **1967**, *12* (3), 287−297.
(31) Sipos, P. M.; Hefter, G.; May, P. M. *J. Chem. Eng. Data* **2000**, *45* (4), 613−617.
(32) Barton, S. S.; Boulton, G. L.; Harrison, B. H. *Carbon* **1972**, *10* (4), 395−400.
(33) Galakhov, V. R.; Demeter, M.; Bartkowski, S.; Neumann, M.; Ovechkina, N. A.; Kurmaev, E. Z.; Logachevskaya, N. I.; Mukovskii, Y. M.; Mitchell, J.; Ederer, D. L. *Phys. Rev. B* **2002**, *65* (11), 113102.
(34) Cramer, S. P.; Degroot, F. M. F.; Ma, Y.; Chen, C. T.; Sette, F.; Kipke, C. A.; Eichhorn, D. M.; Chan, M. K.; Armstrong, W. H.; Libby, E.; Christou, G.; Brooker, S.; McKee, V.; Mullins, O. C.; Fuggle, J. C. *J. Am. Chem. Soc.* **1991**, *113* (21), 7937−7940.
(35) Vanderlaan, G.; Kirkman, I. W. *J. Phys.: Condens. Matter* **1992**, *4* (16), 4189−4204.
(36) de Groot, F. *Chem. Rev. (Washington, DC, U. S.)* **2001**, *101* (6), 1779−1808.
(37) Stobbe, E. R.; de Boer, B. A.; Geus, J. W. *Catal. Today* **1999**, *47* (1−4), 161−167.
(38) Navrotsky, A.; Ma, C. C.; Lilova, K.; Birkner, N. *Science* **2010**, *330* (6001), 199−201.
(39) Shanmugam, S.; Gedanken, A. *J. Phys. Chem. B* **2006**, *110* (48), 24486−24491.
(40) Mao, L. Q.; Zhang, D.; Sotomura, T.; Nakatsu, K.; Koshiba, N.; Ohsaka, T. *Electrochim. Acta* **2003**, *48* (8), 1015−1021.
(41) Lima, F. H. B.; Calegaro, M. L.; Ticianelli, E. A. *J. Electroanal. Chem.* **2006**, *590* (2), 152−160.
(42) Suzuki, N.; Sasaki, H.; Morinaga, Y.; Yamada, Y. *Appl. Surf. Sci.* **2005**, *252* (5), 1498−1501.
(43) Lee, J. S.; Lee, T.; Song, H. K.; Cho, J.; Kim, B. S. *Energy Environ. Sci.* **2011**, *4* (10), 4148−4154.
(44) Tang, Q. E.; Jiang, L. H.; Qi, J.; Jiang, Q.; Wang, S. L.; Sun, G. Q. *Appl. Catal., B* **2011**, *104* (3−4), 337−345.
(45) Wang, Y. G.; Cheng, L.; Li, F.; Xiong, H. M.; Xia, Y. Y. *Chem. Mater.* **2007**, *19* (8), 2095−2101.
(46) Su, H.-Y.; Gorlin, Y.; Man, I. C.; Calle-Vallejo, F.; Nørskov, J. K.; Jaramillo, T. F.; Rossmeisl, J. *Phys. Chem. Chem. Phys.* **2012**, *14* (40), 14010−14022.
(47) Wenchao, S.; Gasteiger, H. A.; Yang, S.-H. *J. Electrochem. Soc.* **2010**, *157* (11), B1529−B1536.
(48) Mayrhofer, K. J. J.; Strmcnik, D.; Blizanac, B. B.; Stamenkovic, V.; Arenz, M.; Markovic, N. M. *Electrochim. Acta* **2008**, *53* (7), 3181−3188.
(49) Brenet, J. P. *J. Power Sources* **1979**, *4* (3), 183−190.
(50) Suntivich, J.; Gasteiger, H. A.; Yabuuchi, N.; Shao-Horn, Y. *J. Electrochem. Soc.* **2010**, *157* (8), B1263−B1268.
(51) Bonakdarpour, A.; Lefevre, M.; Yang, R. Z.; Jaouen, F.; Dahn, T.; Dodelet, J. P.; Dahn, J. R. *Electrochem. Solid State Lett.* **2008**, *11* (6), B105−B108.
(52) Gyenge, E. L.; Drillet, J.-F. *J. Electrochem. Soc.* **2012**, *159* (2), F23−F34.